

This work was written as part of one of the author's official duties as an Employee of the United States Government and is therefore a work of the United States Government. In accordance with 17 U.S.C. 105, no copyright protection is available for such works under U.S. Law.

Public Domain Mark 1.0

<https://creativecommons.org/publicdomain/mark/1.0/>

Access to this work was provided by the University of Maryland, Baltimore County (UMBC) ScholarWorks@UMBC digital repository on the Maryland Shared Open Access (MD-SOAR) platform.

Please provide feedback

Please support the ScholarWorks@UMBC repository by emailing scholarworks-group@umbc.edu and telling us what having access to this work means to you and why it's important to you. Thank you.



Extension of the Energy Range Accessible with a TES Using Bath Temperature Variations

S. Beaumont^{1,2} · J. S. Adams^{1,2} · S. R. Bandler¹ · J. A. Chervenak¹ ·
F. M. Finkbeiner^{1,3} · R. Hummatov^{1,2} · R. L. Kelley¹ · C. A. Kilbourne¹ ·
A. R. Miniussi^{1,2} · F. S. Porter¹ · J. E. Sadleir¹ · K. Sakai^{1,2} · S. J. Smith^{1,2} ·
N. A. Wakeham^{1,2} · E. J. Wassell^{1,4}

Received: 20 August 2019 / Accepted: 8 February 2020 / Published online: 24 February 2020
© Springer Science+Business Media, LLC, part of Springer Nature 2020

Abstract

The energy range of transition-edge sensor (TES) X-ray microcalorimeters with a multiplexed readout depends upon the width and shape of the TES superconducting transition, and also on the dynamic range of the readout. In many detector systems, the multiplexed readout slew rate capability will be the limiting factor for the energy range. In these cases, if we are willing to accept some energy resolution degradation, we can significantly extend the energy range by increasing the bath temperature of operation, essentially creating a second “extended energy range” mode of operation. For example, if we require the very highest energy resolution up to 7 keV, and wish to optimize the design up to this energy, for some measurements it could be very beneficial to have a mode where we can extend the energy range to 15–20 keV even if some energy resolution is sacrificed. In this paper, we explore the trade-off between dynamic range and energy resolution from changing the bath temperature of the TES. We present measurements of TES resolution and slew rate as a function of bath temperature and compare to numerical simulations.

Keywords TES · Energy range · Slew rate

✉ S. Beaumont
sophie.beaumont@nasa.gov

¹ NASA Goddard Space Flight Center, Greenbelt, USA

² CRESST II - University of Maryland Baltimore County, Baltimore, USA

³ Sigma Space Corp., Lanham, USA

⁴ Science Systems and Applications Inc., Lanham, USA

1 Introduction

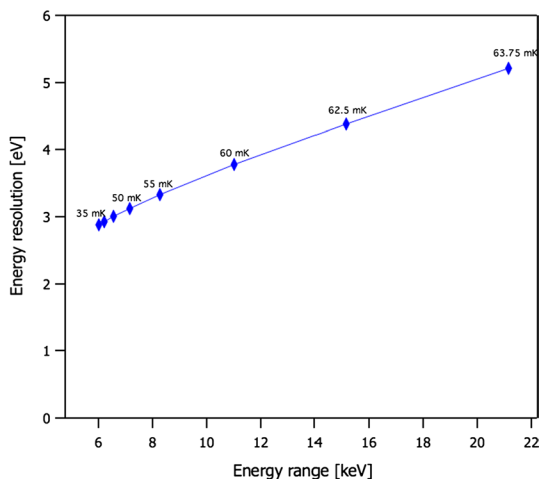
Transition-edge sensor (TES) microcalorimeters are ideal detectors for applications requiring high-resolution X-ray imaging spectroscopy. As such, TES arrays are the baseline detector technology of future X-ray space instruments such as the X-ray Integral Field Unit (X-IFU) instrument on ESA's Athena mission [1] and have also been proposed for the Lynx mission [2] currently under review for National Academy of Science (NAS) 2020 decadal survey. These non-dispersive high-resolution spectrometers are thermistors consisting of superconducting metals that operate in the highly temperature-sensitive transition region between the superconducting and normal metal states. The energy range of the pixel designs depends upon three factors: the total device heat capacity, the shape of the TES superconducting transition, and the maximum slew rate capability of the readout (the slew rate is the derivative of the X-ray current signal with respect to time, $dI/dt|_{\max}$). Current detectors are being designed for an energy range focusing on soft X-rays, up to 7 keV for Lynx or 12 keV for Athena. However, being able to extend this range up to 15 or 20 keV, without reoptimizing the pixel design, could be a major asset for some science studies, such as improving black hole spin measurements or our understanding of the feedback process, as well as of other ultra-luminous X-ray sources.

This is particularly relevant for the multiplexed readout of many pixels with a single readout chain. For the X-IFU, the readout is frequency domain multiplexing (FDM) [3], and the backup readout is time division multiplexing (TDM) [4]. For both of these readout types, in order to stably read out many pixels, the coupling of the input coils from the TESs to the first stage SQUID amplifiers must be small enough, so that the maximum input slew rate (generated by the highest energy X-rays) is small enough to keep the SQUID “error signal” within the quasi-linear flux range of the SQUID. This is required for stable operation within the readout flux-locked feedback loop. As more TESs are multiplexed, with FDM the available bandwidth per pixel is reduced, while with TDM the sampling rate for each pixel decreases. Either way, this leads to the error signals becoming bigger and an increased possibility of losing lock on the SQUIDs. One way to avoid this is to make the SQUID input coupling weaker, at the expense of increasing the input-referred SQUID amplifier noise, and causing some energy resolution degradation. Otherwise, one could reduce the maximum input slew rate (usually by reducing the maximum allowable X-ray energy). Therefore, the lower the maximum slew rate can be (for a given readout noise energy resolution budget), the more pixels can be multiplexed in a single readout column.

The energy range extension could in theory easily be done with minimal changes to the design of the mission (only the innermost X-ray mirrors may need additional coatings to increase the reflectivity for higher energy X-rays), by simply increasing the temperature of the bath, T_b , of the TES. For a given resistive transition shape, increasing T_b reduces the quiescent current required to bias the TES in the transition and reduces the amount of electrothermal feedback (which reduces the detector speed). Both of these effects will reduce $dI/dt|_{\max}$. However,

operating at a higher bath temperature may also negatively affect the energy resolution due to three main affects. Firstly, a higher T_b gives rise to increased thermal fluctuation noise between the TES and the heat bath. Secondly, the TES gain will be more sensitive to thermal fluctuations in T_b , and thirdly, the lower current responsivity of the device may increase the impact of any white noise in the readout chain. A preliminary simulation was done in Bandler et al. [5] in order to evaluate how the estimated energy resolution and energy range might change as a function of the bath temperature (Fig. 1). The simulation assumed a linear TES transition model, which was independent of bath temperature, and only included the effects of the intrinsic detector noise. It should be pointed out that although this simulation assumes a linear transition model which is not rigorously correct, it appears to be a useful initial assumption to explore the basic principles of the studied effects. This simulation was run for a typical TES X-ray microcalorimeter, with a critical temperature $T_C = 65$ mK. The model assumed a slew rate capability sufficient to measure X-rays up to 7 keV and a full-width-half-maximum (FWHM) energy resolution of $\Delta E_{FWHM} = 3$ eV for $T_b = 45$ mK. It also assumes that the limiting factor of the energy range is the slew rate. Under these assumptions, this showed that it is possible to extend the energy range above 15 keV, provided that T_b is increased to just a few mK below T_C . But this also showed that ΔE_{FWHM} is expected to degrade to ~ 5 eV. It hence appeared that, by accepting a degradation in resolution, one could extend the accessible energy range by over a factor of 2. In this work, we perform the associated laboratory measurements required in order to assess the real slew rate variation and energy resolution degradation, and hence the feasibility and potential of this method.

Fig. 1 Plot of the modeled energy range and energy resolution as a function of bath temperature, as it is increased closer to the critical temperature (being here 65 mK) [5] (color figure online)



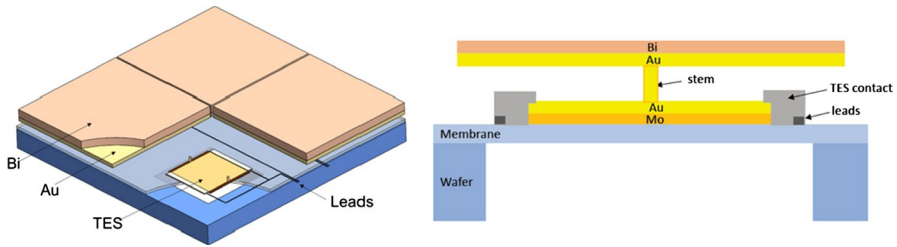
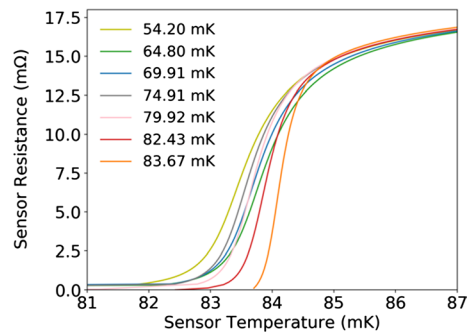


Fig. 2 Scheme of TES detector used for the measurements from above (left) and from the side (right) (color figure online)

Fig. 3 Resistive transitions of our TES for various bath temperatures as a function of temperature (color figure online)



2 Experiment

2.1 Measurements

The TES used in this experiment (Fig. 2) is made of a $\sim 100\text{ }\mu\text{m}$ square Mo/Au bilayer deposited on a $\sim 0.5\text{-}\mu\text{m}$ -thick SiN membrane [6]. The thicknesses of the Mo and Au are, respectively, 35 nm and 172 nm. They have been chosen to yield a T_C of $\sim 90\text{ mK}$ and a sheet resistance of $\sim 40\text{ m}\Omega/\square$. Some discussion regarding typical uniformity properties of those bilayers can be found in [6]. The absorber is $\sim 5.5\text{ }\mu\text{m}$ thick and $\sim 240\text{ }\mu\text{m}$ wide and consists of two electroplated layers of Au and Bi. The absorbers are attached to the TES sensor via two pillar stems. Two banks are deposited at the edge of the TES, parallel to the current flow (not represented on the right scheme of Fig. 2).

We measured $T_C = 86.5\text{ mK}$ under low bias, a thermal conductance of $G_b = 103\text{ pW/K}$ at T_C , and a heat capacity of $C = 1.0\text{ pJ/K}$ at T_C . The normal state resistance of these detectors is $R_n \sim 20\text{ m}\Omega$. Example of sensor resistance R_{TES} versus sensor temperature T_{TES} curves, for different bath temperatures, is shown in Fig. 3. Those curves are derived from current and voltage (I – V) measurements of the TES, where information on thermal parameters from the TES such as G_b is used to extract the sensor temperature. Figure 3 shows that the transition shapes are in fact changing with the bath temperature.

In this experiment, we vary T_b from 55 mK—our usual temperature of operation for this kind of detectors—up to 83.75 mK—in order to get as close as possible to

T_c while still being able to measure a reasonable level of signal to noise. Two different sources of X-rays are in turn placed outside the cryostat, providing X-rays with a count rate of about ~ 1 – 1.5 counts per second. Those sources are an aluminum fluorescence target source, producing X-rays at 1.5 keV (Al-K α) and as a by-product some X-rays at 277 eV (C-K α), and an Fe-55 electron capture source, producing X-rays at 5.9 keV (Mn-K α). The total TES bias circuit inductance including the SQUID input coil and parasitic from wiring is $L=30$ nH. This is much less than the inductance required to critically damp the detectors, and thus, the pulses shapes were operated in an overdamped condition.

2.2 Modeling

The current- and temperature-dependent transition shape $R(I, T)$ of our detector can be described by two key parameters: $\alpha = \frac{T}{R} \frac{\partial R}{\partial T} \big|_I$ and $\beta = \frac{I}{R} \frac{\partial R}{\partial I} \big|_T$. These parameters are derived from measurements of the small signal complex impedance $Z(f)$ (over the frequency range $f=10$ Hz to 5 kHz), measured at $T_b=55$ mK and 82.5 mK [7]. A small signal detector model is then used to calculate pulse shapes (as shown in Fig. 4 for an energy of 1.5 keV). The slew rate is calculated by taking the maximum of the derivative of the simulated pulses. The resulting dI/dt_{\max} is shown in Fig. 5 for both 1.5 keV and 5.9 keV. By fitting a noise model to the measured current noise spectral density (using the procedures described in [7]), one can extract the different detector noise components and calculate the predicted energy resolution from the integration over frequency of the detector noise equivalent power, $NEP(f)$. The modeled integrated $NEP(f)$ is shown in Fig. 5 for an energy of 1.5 keV.

We can observe that α and β , and so the transition shapes, are different at different bath temperatures, unlike the model described in [5] which assumed constant transition shape. This will hence ultimately affect the energy resolution and the slew rate.

From the small signal modeling, a reduction in dI/dt_{\max} by a factor ~ 2 can be expected for operating points above $10\% R_n$ for both energies by increasing T_b from 55 to 82.5 mK. Meanwhile, the predicted resolution from the integrated $NEP(f)$ appears to be degraded by a factor ~ 1.3 between those temperatures. The difference in trend of the slew rates between the two temperatures at low operating points appears to be consistent with the pulse shapes from the zoom on Fig. 4.

3 Measured Slew Rate and Energy Resolution

3.1 Impact of T_b on the Slew Rate

The measured average pulse shapes are plotted in Fig. 6, showing some differences from the pulses modeled in the small signal limit with clear saturation of the top part of the pulses at 5.9 keV. This shows that the measured and modeled pulse heights at $12.5\% R_n$ differ by $\sim 20\%$ for 1.5 keV, while it changes by $\sim 50\%$ at 6 keV. A zoomed version of the pulses (also in Fig. 6) shows that the data were a bit under-sampled, but could still lead to a measurement of the slew rate despite some noise in the data,

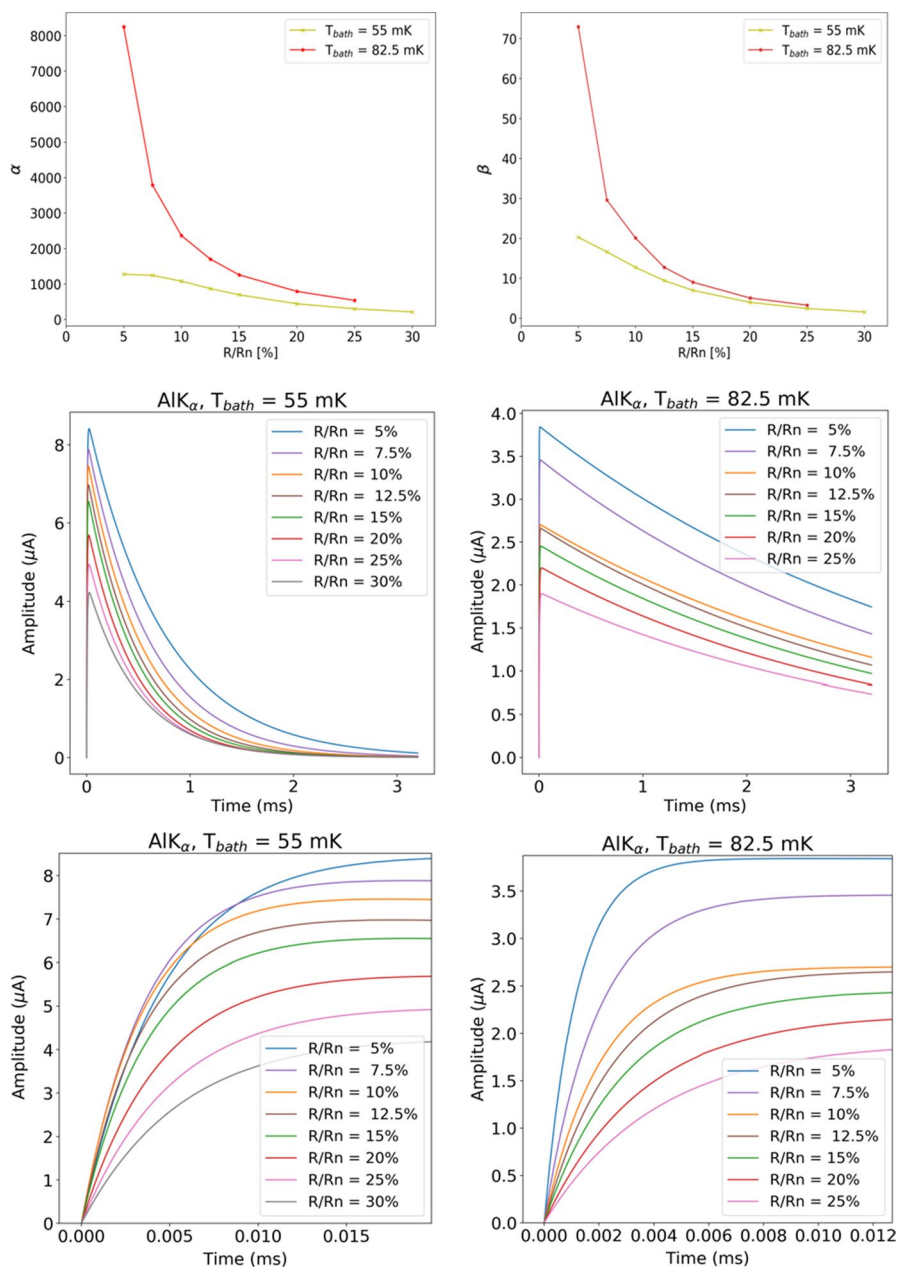


Fig. 4 Plots of α (top left) and β (top right) for bath temperatures of 55 mK and 82.5 mK as a function of the bias point. (Middle) Plot of the corresponding simulated pulses at a bias point of 12.5% R_n for an energy of 1.5 keV (Al-K α line), with a zoomed version on the rise of the pulse (bottom) (color figure online)

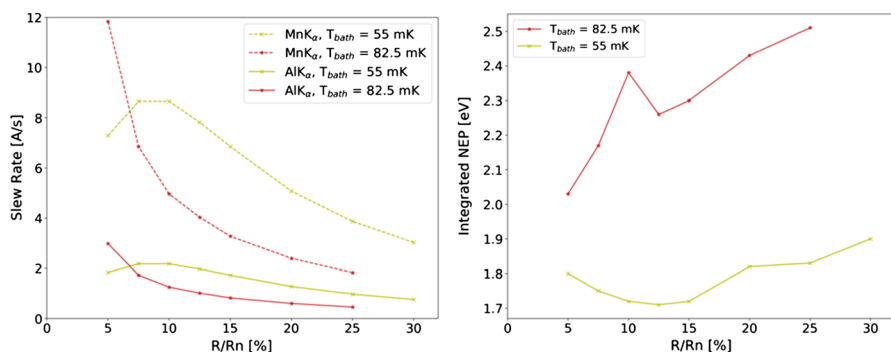


Fig. 5 (Left) Plot of the simulated slew rates as a function of the operating point, for bath temperatures of 55 mK and 82.5 mK for both 1.5 and 5.9 keV. (Right) Plot of the predicted NEP as a function of the operating point, for bath temperatures of 55 mK and 82.5 mK for 1.5 keV (color figure online)

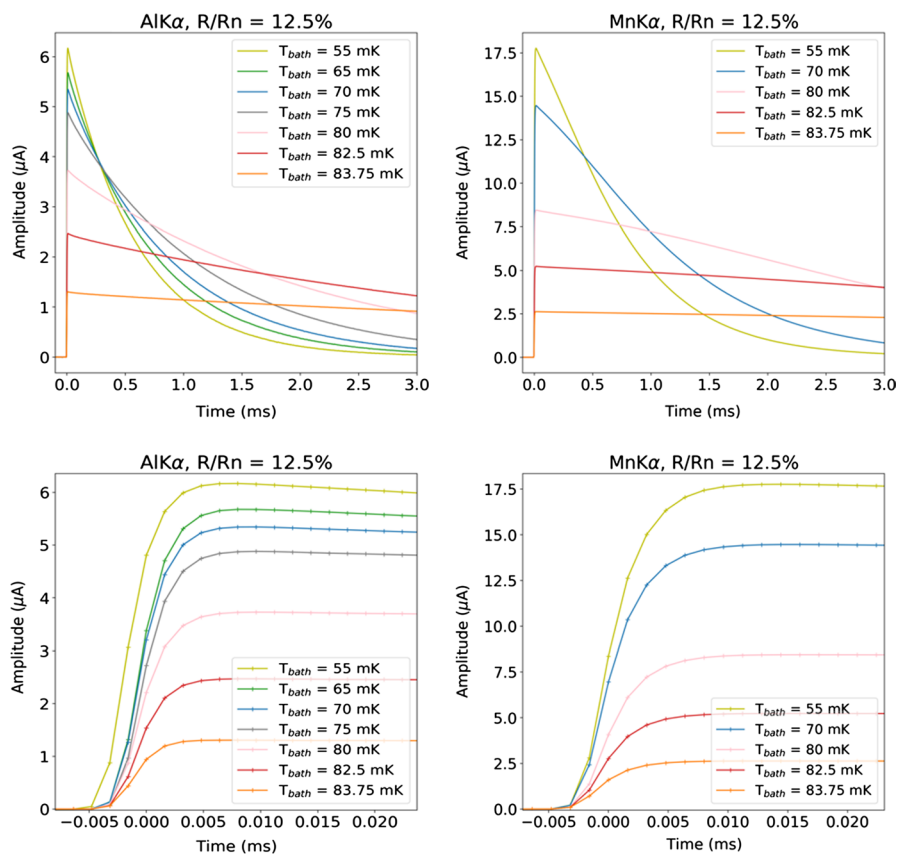


Fig. 6 Plots of the measured average pulse shapes at the operating point $12.5\% R_n$ for various bath temperatures, at 1.5 keV ($AlK\alpha$ line) (top left) and 5.9 keV ($MnK\alpha$) (top right). Zooms over the beginning of the pulses are also shown (bottom) (color figure online)

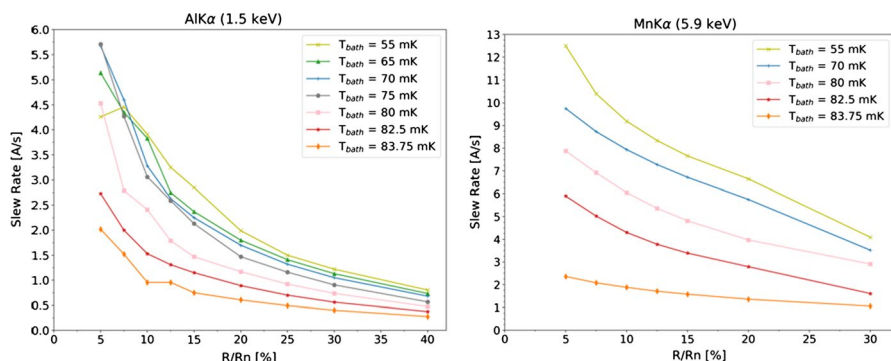


Fig. 7 Maximum measured slew rate for Al-K α (left) and Mn-K α (right) X-rays as a function of the bias point, for various bath temperatures (color figure online)

especially visible at low operating points for Al-K α . The slew rate (see Fig. 7) is derived analytically from a model of the pulses fitted to the data. This includes a correction of a low-pass filter used in the data acquisition digitizer.

As we increase the T_b , we observed a decrease in the $dI/dt|_{\max}$ for any operating point above 10% R_n . At 1.5 keV, we observe a decrease by a factor ~ 2.4 and ~ 3.4 in the slew rate by increasing the bath temperatures from 55 to 82.5 and 83.75 mK, respectively. At 5.9 keV, this factor is around ~ 2.2 when increasing the T_b from 55 to 82.5 mK and becomes closer to a factor ~ 4.8 when going up to 83.75 mK. The difference between behaviors at 1.5 and 5.9 keV is likely due to the change in non-linearity for different bath temperatures.

3.2 Impact of T_b on the Resolution

Together with the average pulse shapes, measurements of the average noise spectral density were taken for various R/R_n and T_b , from which the resolution from the integrated NEP(f) is calculated (see Fig. 8).

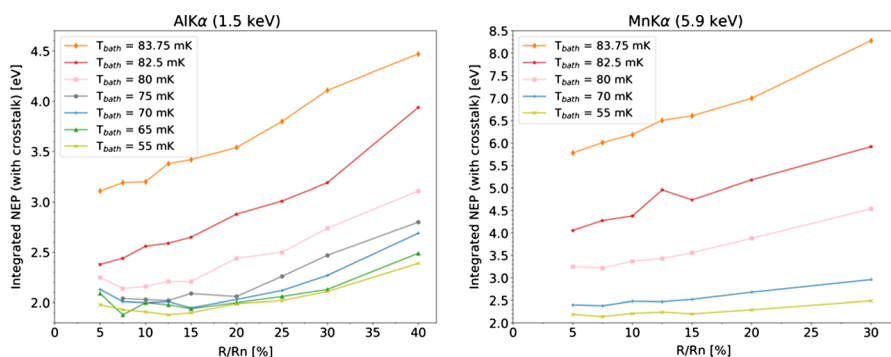


Fig. 8 Integrated NEP(f) at 1.5 keV for Al-K α (left) and 5.9 keV Mn-K α (right) as a function of the bias point, for various bath temperatures (color figure online)

As we increase the bath temperature, we observed an increase in the integrated NEP(f) values. This is in general expected because of the higher thermal fluctuation noise with increasing T_b . We measure a degradation in the integrated NEP at 12.5% R_n by a factor ~ 1.5 and ~ 1.8 at 1.5 keV going from 55 to 82.5 and 83.75 mK, respectively. At 5.9 keV however, we observe factors of ~ 2.2 and ~ 2.8 going from 55 to 82.5 and 83.75 mK, respectively.

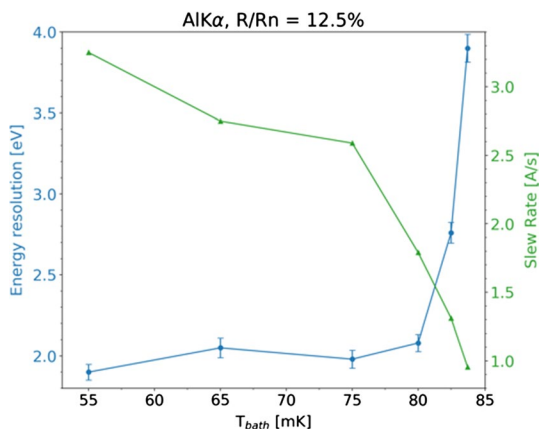
We measured an Al-K α energy histogram from ~ 5000 X-ray pulses for various bath temperatures at a single bias point of 12.5% R_n . The fitted ΔE_{FWHM} and dI/dI_{max} are plotted as a function of T_b on Fig. 9.

4 Discussion

From a consideration of the energy resolution for the aluminum source as a function of T_b together with the measured slew rate, it is clearly evident that an extended energy range mode with an elevated bath temperature could potentially be very useful. The value of such a mode requires a trade-off of how much degradation there is in energy resolution versus the increase in energy range that the increased slew rate affords. For this particular dataset, the slew rate decreases rapidly above 75 mK, while the energy resolution also degrades quickly.

The energy resolution degradation was not measured at 5.9 keV, but based upon the pulse shapes and integrated NEPs, we would expect the deterioration to be larger than we observed at 1.5 keV. Indeed, as we go higher in energy and also higher in temperature, the shapes of the pulses change more as the resistance gets closer to the normal resistance. This can be due to a reduction in the steepness of the transition, and also due to the current signal in the SQUID readout starting to saturate due to the nonlinear bias circuit [8]. This nonlinearity in pulse shape can explain some of the differences observed between the actual and modeled data, which are reasonably consistent at 1.5 keV but become less consistent at 5.9 keV. The change in pulse shape can be observed in Fig. 10, where the pulse shapes for C-K α , Al-K α and Mn-K α are shown on a logarithmic scale, normalized by dividing each pulse shape

Fig. 9 This plot shows the changes in energy resolution and slew rate for various bath temperatures at a constant bias point that is 12.5% of R_n for Al-K α (color figure online)



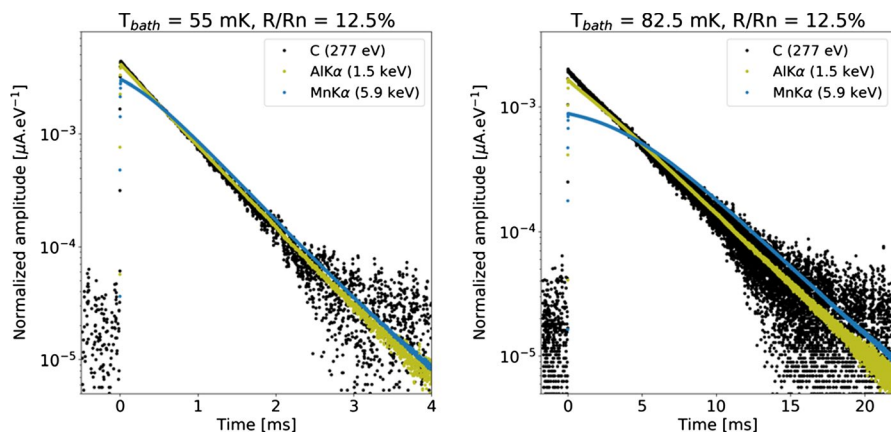


Fig. 10 Plot of the pulse shapes normalized by their respective energy of the X-ray for carbon lines measured together with Al-K α and Mn-K α , at 55 mK (left) and 82.5 mK (right) (color figure online)

with average K α energy. The effects of saturation and nonlinearity are fairly small for the Al-K α both at 55 and at 82.5 mK, but are more clearly visible for Mn-K α at 55 mK and even more obvious for Mn-K α at 82.5 mK.

It is interesting to note that there is an offset in pulse decay for Mn-K α after approximately 10 ms compared with the pulse shapes for C or Al-K α . This offset does not impact the slew rate, but can be explained by the effects of the nonlinearity. For the largest signals, there is an increase in the change of α and β during the pulse. With larger signals, the energy removed from the TES by electrothermal feedback (i.e., by a reduction in the bias power) becomes less, and this leads to a small measurable offset in the pulse-shape decay without impacting the time constant. This interpretation is consistent with there being almost no offset between the pulse decays of C and Al-K α , which are both reasonably linear.

Furthermore, from the curves in Fig. 7, it is natural to ask what impact the bias point has on the slew rate, and whether simply changing the bias point is any better or worse for the energy resolution than changing the bath temperature in order to reduce the maximum slew rate. In Fig. 11, both the integrated NEP(f) and dI/dI_{\max} at 55 mK have been plotted as a function of the bias point. This plot shows that dI/dI_{\max} can indeed be reduced by a significant factor by increasing the operating point. At 1.5 keV, a reduction by a factor ~ 2.6 or ~ 4 in dI/dI_{\max} can be achieved by increasing the operating point from 12.5 to 30% or 40% R_n , respectively, and also causing a degradation in the integrated NEP(f) by a factor ~ 1.2 or ~ 1.3 , respectively. At 5.9 keV, a reduction in dI/dI_{\max} by a factor ~ 2 can be achieved by increasing the operating point from 12.5 to 30% R_n , with a degradation in integrated NEP(f) of a factor ~ 1.1 .

This approach therefore looks promising as a means to reducing the maximum slew rate and should be investigated further with more measurements. However, it should be emphasized that the degradation in performance here is only considered through integrated NEPs, as no spectrum has so far been acquired for bias

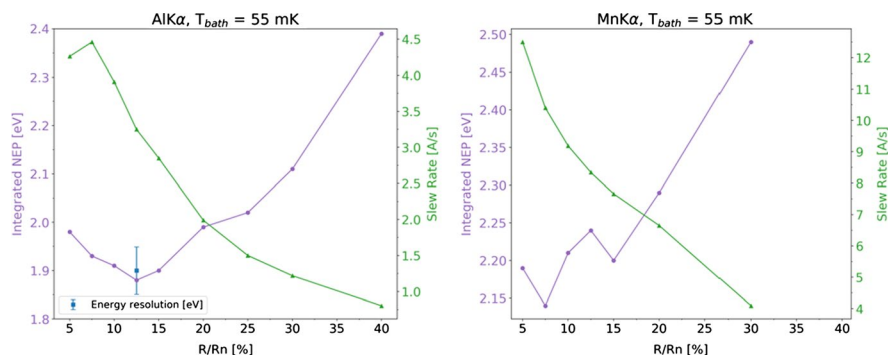


Fig. 11 Plot showing the changes in integrated NEP and slew rate for various operating points at $T_b = 55$ mK, for both Al-K α (left) and Mn-K α (right). For Al-K α , a measure of the energy resolution at 12.5% R_n is also shown for reference (color figure online)

points higher than 12.5%, and in this approach, the available change in resistance is inherently less than using the approach of changing the bath temperature while maintaining the same biased operating point. Appropriate measurements of the energy resolution would hence be of a major importance in order to properly assess the potential of this alternative option.

5 Conclusion

Based upon previous simulations, one might expect that it is relatively straightforward to increase the energy range of an X-ray microcalorimeter by increasing the bath temperature of operation, and reducing the bias power to remain at the same bias point, if the energy range is limited by the readout maximum slew rate capability. In this work, we have investigated this process and described some of the challenges that are associated with this approach. Our experiment has confirmed that for the particular X-ray microcalorimeter design that we investigated, the maximum slew rate and thus potentially the energy range can indeed be extended by operating at higher bath temperature at the cost of a degradation of the energy resolution, as expected. We have observed, for example, that a reduction in slew rate by a factor of up to ~ 3.4 can be achieved when the energy resolution is degraded by a factor ~ 2.1 , from measurements of 1.5 keV X-ray. Further studies could investigate the possible effects of increased susceptibility to bath temperature fluctuations, and the possible impact on resolution of increased multiplexed readout noise. If future TESs were designed for this type of multimodal operation for the different energy ranges, it would be advantageous to have a design that has relatively broad transitions in order to be less affected by nonlinearity.

References

1. D. Barret et al., The Athena X-ray Integral Field Unit (X-IFU), in *Proceedings of SPIE Space Telescopes and Instrumentation 2016: Ultraviolet to Gamma Ray*, vol. 9905 (2016), p. 99052F
2. J.A. Gaskin et al., *J. Astron. Telesc. Instrum. Syst.* **5**(2), 021001 (2019). <https://doi.org/10.1117/1.JATIS.5.2.021001>
3. J. van der Kuur et al., Optimising the multiplex factor of the frequency domain multiplexed readout of the TES-based microcalorimeter imaging array for the X-IFU instrument on the Athena x-ray observatory, in *Proceedings of SPIE*, vol. 9905 (2016), p. 99055R
4. W.B. Doriese et al., Developments in time-division multiplexing of x-ray transition-edge sensors. *J. Low Temp. Phys.* **184**, 389–395 (2016)
5. S.R. Bandler et al., *J. Astron. Telesc. Instrum. Syst.* **5**(2), 021017 (2019). <https://doi.org/10.1117/1.JATIS.5.2.021017>
6. F.M. Finkbeiner et al., Electron-beam deposition of superconducting molybdenum thin films for the development of Mo/Au TES X-ray microcalorimeter. *IEEE Trans. Appl. Supercond.* **27**(4), 1–4 (2017)
7. N. Iyomoto et al., Modeling of TES X-ray microcalorimeters with a novel absorber design. *J. Low Temp. Phys.* **151**(1–2), 406 (2008)
8. P. Peille et al., Performance assessment of different pulse reconstruction algorithms for the ATHENA X-ray Integral Field Unit, in *Proceedings Volume 9905, Space Telescopes and Instrumentation 2016: Ultraviolet to Gamma Ray* (2016), p. 99055W. <https://doi.org/10.1117/12.2232011>

Publisher's Note Springer Nature remains neutral with regard to jurisdictional claims in published maps and institutional affiliations.